Communications Materials

https://doi.org/10.1038/s43246-026-01121-0

Article in Press

Cr-LiF as a high energy density conversion-type cathode for Li-ion solid-state batteries

Received: 3 October 2025

Accepted: 19 February 2026

Cite this article as: Casella, J., Morzy, J., Montanelli, V. *et al.* Cr-LiF as a high energy density conversion-type cathode for Li-ion solid-state batteries. *Commun Mater* (2026). https://doi.org/10.1038/s43246-026-01121-0

Joel Casella, Jędrzej Morzy, Vittorio Montanelli, Felix C. Mocanu, Arnold Müller, Moritz H. Futscher, Marta D. Rossell, M. Saiful Islam, Maksym Yarema & Yaroslav E. Romanyuk

Cr-LiF as a High Energy Density Conversion-Type Cathode for Li-ion Solid-State Batteries

Joel Casella,[*,†] Jędrzej Morzy,[†] Vittorio Montanelli,[‡] Felix C. Mocanu,[¶] Arnold Müller,[§] Moritz H. Futscher,[†] Marta D. Rossell,[‡] M. Saiful Islam,[¶] Maksym Yarema,[‖] and Yaroslav E. Romanyuk[*,†]

†*Laboratory for Thin Films and Photovoltaics, Empa - Swiss Federal Laboratories for Materials Science and Technology, Dübendorf, 8600, Switzerland*

‡*Electron Microscopy Center, Empa - Swiss Federal Laboratories for Materials Science and Technology, Dübendorf, 8600, Switzerland*

¶*Energy Materials Research Group, Department of Materials, University of Oxford, Oxford, OX1 3PH, United Kingdom*

§*Laboratory of Ion Beam Physics, ETH Zürich, Zürich, 8093, Switzerland*

‖*Institute for Electronics, Department of Information Technology and Electrical Engineering, ETH Zürich, Zurich, 8092, Switzerland*

E-mail: joel.casella@empa.ch; yaroslav.romanyuk@empa.ch

Abstract

Transition-metal fluorides (TMFs) are attracting attention as alternative lithium-ion battery cathodes, primarily focusing on Fe-based systems. Here, we report chromium as a previously unexplored transition metal (TM) for TMF cathodes in rechargeable lithium batteries. Utilizing a thin-film solid-state platform, we mitigate the common shortcomings of TMF cathodes, such as sluggish kinetics and electrolyte incompatibility. Coevaporation of Cr and LiF produces a heterogeneous thin film of Cr-LiF

with a 1.1:2 stoichiometric ratio, delivering an initial capacity of 435 mAh/g and an energy density of 0.71 Wh/g at a C/10 cycling rate. Experimental measurements and first-principles calculations identify CrF_2 as the dominant delithiated phase. The cathode maintains a capacity of 208 mAh/g at both 1C and 5C discharge rates after 1500 cycles. Compared to Fe-LiF (FeF_2) analogues, Cr-LiF demonstrates a higher rate capability with 0.255 Wh/g at 3.80 W/g. This work introduces chromium fluorides as a new high-energy conversion cathode, expanding the options of viable positive electrode materials for next-generation batteries.

Keywords

Li-ion battery, solid-state battery, thin-film, chromium fluoride, conversion cathode, LiPON, battery, chromium

1 Introduction

While typical intercalation cathodes for Li-ion batteries, such as $Li(Ni_xMn_yCo_z)O_2$ (NMC), $LiCoO_2$, and $LiFePO_4$ (LFP) reach their physicochemical performance limits, efforts are being made to identify new cathode active materials with higher energy densities.[1,2] Conversion cathodes offer considerable promise in terms of capacity and energy density, while utilizing abundant resources (Supplementary Table 1).[3–6] In particular, transition metal fluorides (TMFs, TM=Mn, Fe, Co, Ni, Cu, ...) offer up to three times the gravimetric capacity of common intercalation-type cathodes, and keeping reasonably high theoretical voltages (2.0-3.5 V).[2,7,8]

By far, the most well-studied TMF cathodes are iron- and copper-based.[9–11] The iron and copper cathodes exhibit capacities of 570 mAh/g and 450 mAh/g (delithiated) in their first cycles, respectively; however, many cases demonstrate poor reversibility.[12,13] The research community is also shifting towards more complex TMF compositions to leverage catalytic

effects that enhance TMF cathode performance.[11] Cu-Fe fluorides are frequently mixed for this purpose, resulting in more stable cycling performance and capacities of up to 500 mAh/g (delithiated).[9,14,15] The combination of copper and iron (x=2 or 3) with carbon has also been explored, showing cycling stability with capacities reaching up to 400 mAh/g (lithiated).[16–18] Nickel and Iron synergies have been shown by Wu et al., achieving 600 mAh/g and decreased charging overpotentials.[19] Wei et al. demonstrate conversion of LiF using a spinel oxide redox host with 237 mAh/g and 88 % voltaic efficiency.[20] In our previous work, we present a Fe-LiF thin-film cathode, tested in a solid-state battery with 480 mAh/g after 2000 cycles.[21]

Chromium (Cr), a light and relatively abundant transition metal, has not yet been investigated as a TMF cathode material. This is likely due to concerns about its toxicity, particularly Cr (VI), which is a known carcinogen.[22] In the context of this work, only metallic Cr is handled (alongside LiF) and it is unlikely that CrF_6 forms.[23,24] In contrast, other oxidation states, such as Cr(III), are not considered toxic and are even biologically essential.[22] The expected redox reaction of Cr-LiF cathode lithium storage is shown in Equation 1.

$$Cr + xLiF \underset{discharging}{\overset{charging}{\rightleftharpoons}} CrF_x + xLi \quad (1)$$

The thermodynamic potential described in Equation 1 is 2.13 V for x = 2 and 2.30 V for x = 3.[25,26] Although not a particularly high voltage cathode, with a lithiated capacity of 516 mAh/g for x = 2 and 619 mAh/g for x = 3, the specific cathode energies that can be achieved are 1.10 Wh/g and 1.42 Wh/g for x = 2 and 3, respectively. These values exceed the capacities deliverable by commonly used intercalation cathodes (∼220 mAh/g and ∼0.8 Wh/g for NMC).[2] When considering only the mass of the transition metal fluoride (TMF) in its delithiated state (e.g., CrF_x), as frequently reported in the literature, the theoretically attainable capacities are 591 mAh/g for x = 2 and 737 mAh/g for x = 3, leading to energies of 1.26 Wh/g and 1.70 Wh/g, respectively.

Despite their promise, TMFs are faced with a new set of challenges for widespread use

in Li-ion batteries. That is, their incompatibility with typical liquid electrolytes, due to particle fusion, active material dissolution, and electrolyte decomposition.[6] Furthermore, TMF conversion cathodes exhibit slow kinetics due to the poor conductivities associated with the TM fluoride phase (delithiated state). The chemical reaction and phase change between TM+LiF and the TMF often bring with it high overpotentials and large volume changes. We have shown in our previous work that many of these challenges can be mitigated by using a thin-film solid-state configuration.[21] Using thin films, cathodes can be tested without cathode additives (binder, carbon black, etc.) and liquid electrolytes, avoiding unwanted side reactions that can skew electrochemical results. In this work, a thin-film battery with a LiPON electrolyte and Li-metal anode was used to study the fundamental properties of the Cr-LiF cathode.

The thin-film solid-state architecture used in this work serves as a model system. As previously mentioned, TMF cathodes have been studied in bulk composite configurations with more conventional solid-state electrolytes and cell designs.[9,27–29] Therefore, we anticipate that the chromium fluoride cathode would behave similarly to other TMF cathodes when incorporated in conventional solid-state electrodes, yet this must be verified experimentally.

2 Results and Discussion

Coevaporation of metallic Cr and LiF was used to manufacture the Cr-LiF cathodes. Such a procedure produces a well-mixed heterogeneous thin film of the two phases with a tunable stoichiometric ratio. In this way, the lithiated (discharged) version of the cathode can be made, which provides inherent benefits to eventual cell implementation (Li-reservoir free, more stable and non-toxic materials, etc.). Supplementary Figure 1 shows the cycling performance of various Cr:LiF ratios. The tested ratios range from 1:1 to 1:3 (Cr:LiF). Through C/10 cycling, Cr-LiF with a stoichiometric ratio of 1.1:2 (Cr:LiF) was identified as having the highest capacity and hence used for further testing and characterization. All cathodes

were tested with 75 nm equivalent pure LiF to have the same capacity. The selected Cr:LiF 1.1:2 cathode has a total measured thickness of 115 nm. This thickness was used to ensure that, despite the low conductivity of the cathode, it can be fully utilized with manageable overpotentials.

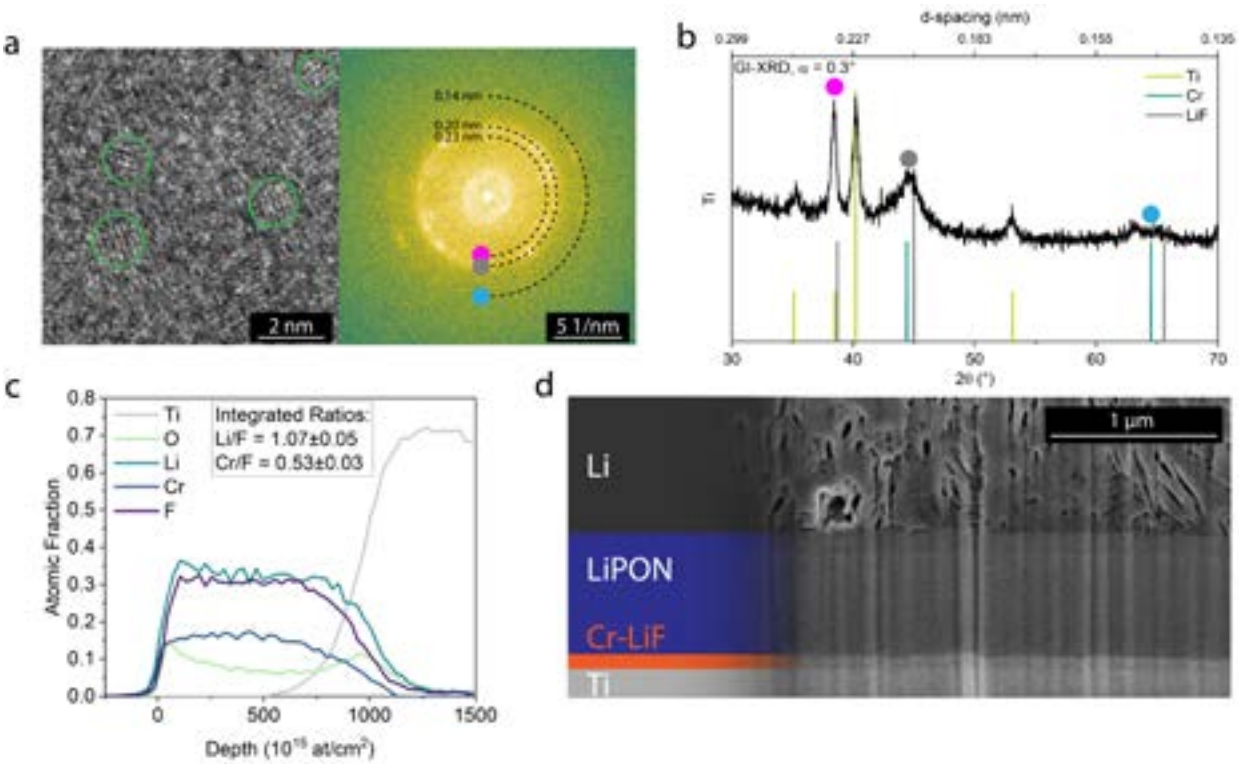

Figure 1: **Cr-LiF cathode and solid-state cell structure (a)** HR-TEM and respective FFT of the as-deposited Cr-LiF cathode. Green circles highlight nanocrystal domains ∼1.5 nm in size. **(b)** GI-XRD pattern of Cr-LiF ($\alpha = 0.3°$). Colored dots are corresponding peak positions from FFT (panel (a)). Reference reflections are taken from ICSD (ICSD release 2025.1).[30] **(c)** 13 MeV ^{127}I ERDA depth profile of pristine cathode. Calculated atomic ratios are also shown. **(d)** FIB-SEM cross section of full cell stack.

Figure 1(a) shows a high-resolution transmission electron micrograph (HR-TEM) of the cathode in its deposited state. The cathode structure shows finely intermixed crystalline phases with some amorphous regions. The fast Fourier transform (FFT) of the HR-TEM shows the polycrystalline rings with expected d-spacing. However, the Cr (Im-3m) and LiF (Fm-3m) structures are similar and difficult to distinguish. The same conclusion can be drawn from the grazing-incidence X-ray diffraction (GI-XRD, $\alpha = 0.3°$), where the same

phases are confirmed (colored dots, Figures 1 (a) and 1 (b)) along with the reflections of the Ti current collector. Figure 1(c) shows an elemental distribution depth profile given by the measurement of the 13 MeV ^{127}I time-of-flight elastic recoil detection analysis (ERDA). In the pristine state, the atomic concentrations of Cr, Li, and F are constant through the 115 nm film. Furthermore, a quantitative analysis of the ratio measures an average ratio of Cr:F of 0.53±0.03:1, confirming the intended ratio of Cr:LiF is 0.55:1 (or 1.1:2). A slight overstoichiometry of Li vs F of 1.07±0.05:1 is within the accuracy expected from the measurement. Figure 1(d) is a cross-sectional SEM micrograph of the entire cell stack, including the cathode (Cr:LiF 1.1:2, 115 nm), 1000 nm LiPON (electrolyte) and 2000 nm Li metal (anode and reference).

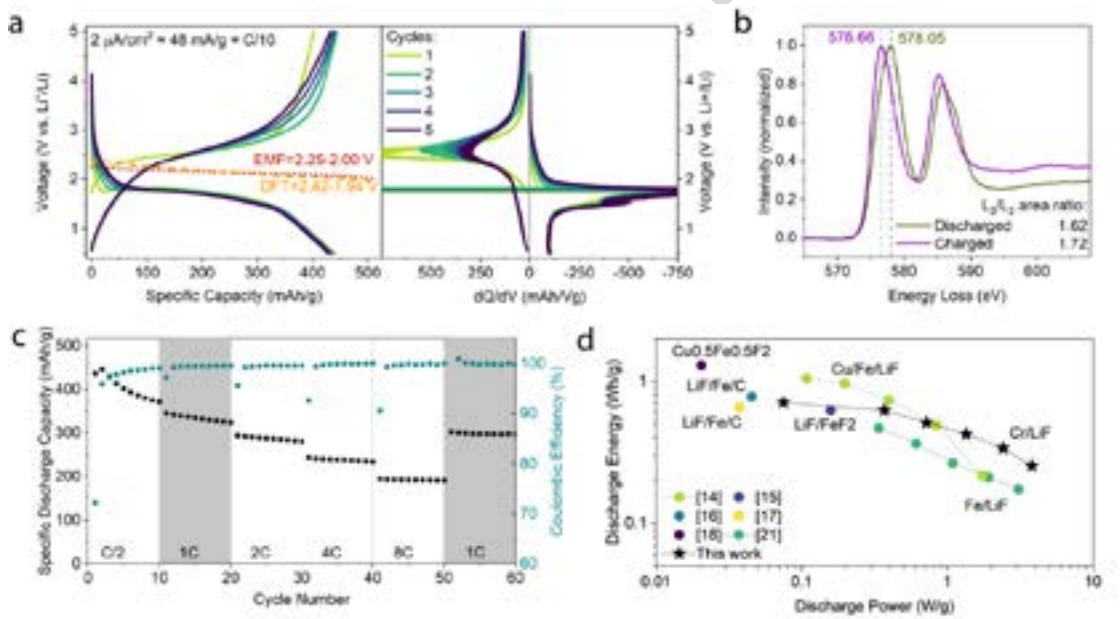

Figure 2: **Electrochemical characterization (a)** Charge-discharge and dQ/dV vs V curves of the first five cycles (2 $\mu A/cm^2$, ∼C/10, 48 mA/g). The dotted red line and dashed orange line represent Nernst relationship voltage profiles calculated from tabulated EMF values and DFT, respectively. **(b)** Representative EEL spectra of the Cr L_3/L_2 edge obtained by averaging 2400 spectra across an area of ∼3600 nm^2 in the center of the discharged (green) and charged (purple) cathodes. For clarity, the spectra are normalized to the intensity of the L_3 peak. Vertical gray lines are a guide to the eye to indicate the fitted Cr L_3 peak positions, separated by ∼1,4 eV. **(c)** Specific discharge capacity vs cycle number at current densities of 10 to 160 $\mu A/cm^2$ (C/2 to 8C assuming 20 $\mu Ah/cm^2$). **(d)** Ragone plot of Cr-LiF cathode compared to literature shown at the lithiated cathode level.[14–18,21]

Figure 2(a) shows the C/10 cycling voltage profiles of the battery cell and the differential capacity (dQ / dV vs. V) for the first five cycles. The dotted/dashed lines represent the bulk thermodynamic voltage profiles for this cathode material. The dashed orange voltage profile uses energies calculated with density functional theory (DFT) at the meta-GGA level.[31] This was performed by evaluating the DFT energies for a selection of relevant structures (see Figures S2, S3 and Table S2). Considering these bulk structures, the free-energy was minimized through 100 steps of lithiation using a grand canonical linear programming approach.[32] Importantly, through this step of minimization of DFT energy, it was determined that only Cr, LiF, and CrF_2 form in the relevant stoichiometric ratio (Table S2 and Supplementary Figure 3). Our free-energy calculations using DFT are only valid for the bulk phases at 0 K and ignore thermal and nanostructure effects. Other phases such as Li3CrF6 might also stabilize under experimentally relevant conditions depending on the details of the nanostructure. The theoretical voltage profile (dotted red) was calculated through tabulated EMF values for Cr^{2+}/Cr versus Li^+/Li.[26] The EMF and DFT values applied to the Nernst equation show that the cathode should provide 2.25-2.00 V and 2.42-1.94 V, respectively, throughout discharge, indicating good accord. The experimentally determined curves show a deviation from these curves, due to overpotentials associated with the kinetics of the cathodes.[2,33–35]

The theoretical lithiated capacity of this cathode is 516 mAh/g (591 mAh/g, delithiated), and in Figure 2 (a) a specific lithiated capacity of 435 mAh/g (498 mAh/g, delithiated) is observed. During the fifth cycle, the average voltage of the charge and discharge half cycles was 2.72 and 1.60 V, respectively, resulting in a voltaic efficiency of 58.8 %.

Through the differential capacity plot in Figure 2(a), a single charging step can be observed. During discharge a voltage "bounce-back" in the first cycles is apparent, as evidenced by the horizontal line in the differential capacity plot at 1.76 V. This phenomenon is known to occur for conversion reactions and indicates an activation of the cathode (reduction of overpotentials) upon the initial lithiation.[34,35] In addition, the discharge occurs through two voltage steps, the majority of the capacity coming at 1.74 V with a smaller contribution at

1.50 V. The charge/discharge asymmetry is also apparent through operando galvanostatic EIS (GEIS), shown in Supplementary Figure 4 and discussed in more detail in Supplementary Note 1. Also, the vertical part shown in the differential capacity graph during discharge below 1 V can be attributed to interfacial storage mechanisms due to small particle sizes (Figure 1(a)) and thus high grain boundary content.[36,37] The experimentally determined 2-step discharge pathway does not follow the bulk DFT energy minimization that suggests a single step reaction (Supplementary Figure 3). However, in this calculation, entropic effects, kinetically stabilized phases, and grain boundary interactions are not considered. It is entirely possible that some intermediate phases, such as the ternary Li_3CrF_6 are stabilized due to the reaction environment and (de)lithiation kinetics.

Figure 2(b) shows electron energy loss spectra (EELS) for the cathode in the charged and discharged states. The L_3 peak exhibits a chemical shift from 578.0 (green) to 576.7 eV (purple) between discharged and charged states, respectively. In addition, the L_3/L_2 area ratio, calculated using the Pearson method,[38] increases from 1.62 in the discharged state to 1.72 in the charged state. A decrease in the L_3 peak energy accompanied by an increase in the L_3/L_2 ratio is indicative of Cr^{2+}, as reported in Ref.[39] These observations are consistent with the DFT-calculated structures, which also predict the formation of CrF_2 upon delithiation.

Figure 2(c) shows the results of the rate testing performed on this cathode. The cycling was carried out at rates from C/2 to 8C (theoretical C rates) for 60 cycles. This translates to current densities of 10 to 160 $\mu A/cm^2$ (cathode loading of 20 $\mu Ah/cm^2$). At C/2 there is evidence of cathode degradation, but the capacity remains high at roughly 400 mAh/g (lithiated). At the highest rate tested of 8C, the cathode-level specific discharge capacity is 192 mAh/g (lithiated), indicating a 48% utilization of the cathode at 8C (compared to C/2 cycling). By comparing the 1C cycling sets (shaded regions) before and after the 2C, 4C, and 8C steps, a capacity fade from an average of 334 mAh/g (before) to 297 mAh/g (after) is observed. The final ten 1C cycles show little capacity loss, indicating that the degradation

mechanism may be self-limiting, which will be discussed in more detail later.

Figure 2(d) shows a Ragone plot comparing the Cr-LiF cathode developed here to other TMF cathodes in previous studies.[14–18,21] For completeness, both thin-film and bulk cathodes have been shown. Cr-LiF shows cathode level specific discharge energies from 0.707 to 0.255 Wh/g and respective specific discharge powers of 0.075 to 3.80 W/g. Considering the voltage profile from DFT shown in Figure 2(a), which predicts a lithiated cathode level energy of 0.991 Wh/g, the cathode achieves 71.3% of theoretical energy at our lowest charging rate of C/10. In comparison to literature, the Cr-LiF cathode outperforms the others at higher powers.

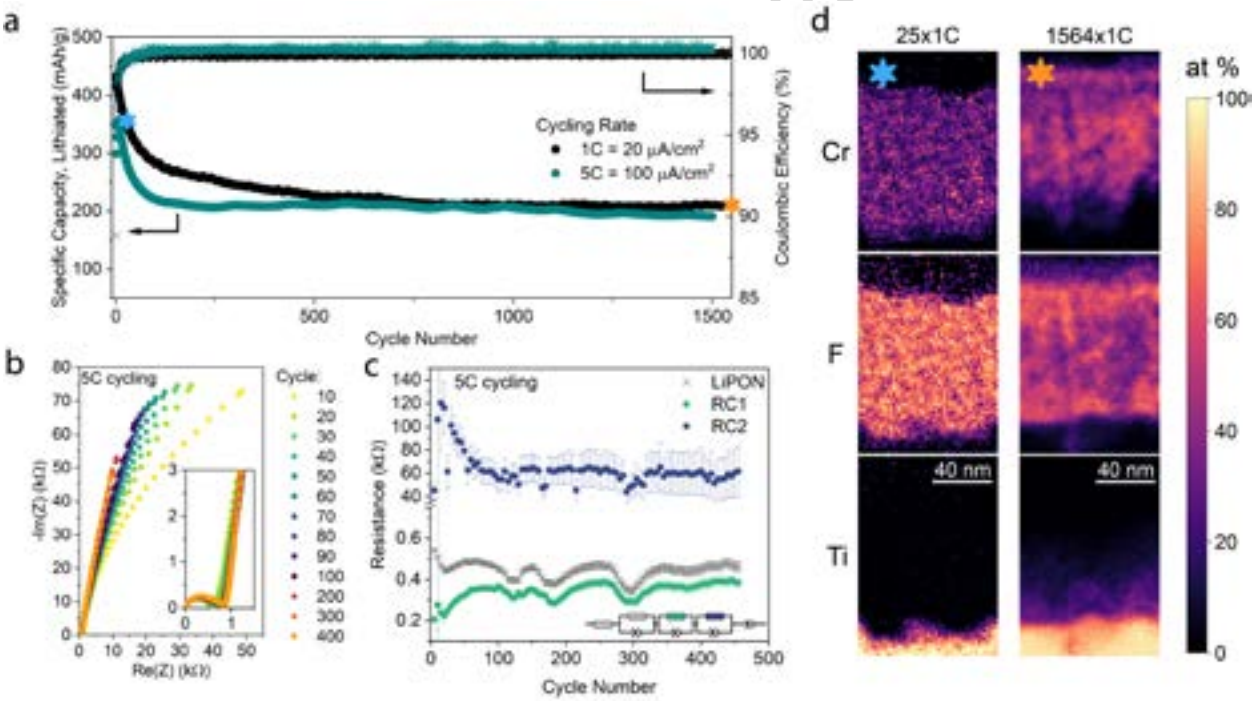

Figure 3: **Long term behavior (a)** Specific discharge capacity vs cycle number for a Cr-LiF cathode cycled at 1C (black) and 5C (teal). Coulombic efficiency is shown for all cycles on the right axis. **(b)** Nyquist representation of PEIS spectra taken after different cycle numbers. **(c)** Resistance vs cycle number for fitted resistance values of the LiPON, RC1, and RC2 contributions. The equivalent circuit used to fit the PEIS spectra is shown. Error bars represent ±1 standard error of the fitted values. **(d)** STEM-EDX maps of Cr, F, and Ti for samples after 25 cycles and 1564 cycles at 1C (shown as stars on panel (a)). Cycling behavior of 25 cycles is shown in Supplementary Figure 5.

Figure 3(a) shows the results of long-term cycling of the Cr-LiF cathode at 1C and 5C

for 1564 and 1500 cycles, respectively. During 1C cycling, the cathode discharge specific capacity gradually decreases from 433 mAh/g in the first ∼1000 cycles and then stabilizes at 209 mAh/g (average coulombic efficiency in the last 500 cycles is 99.975%). At 5C, the specific capacity peaks at 357 mAh/g in cycle 5. The capacity drops within the first 200 cycles to 208 mAh/g, which is similar to the final capacity shown for the 1C cycling. This suggests the gradual formation of a new cathode structure or phase that can achieve high rates with little extra overpotentials albeit with about half of the initial capacity. This new phase is achieved earlier during 5C cycling. The intrinsic nature of conversion cathodes is known to be highly dependent on cycling rate.[21] Notably, how the internal interfaces are managed (between Cr and LiF for example) can have a significant impact on the kinetic performance of such a cathode but also on their accessible and practical capacity. We speculate that a stable cathode nanostructure forms after ∼1000 1C cycles or ∼200 5C cycles where kinetics are improved but capacity is reduced. The differential capacity plots are shown in Supplementary Figure 6 for a selection of cycles from 25 to 1500 (at 1C). As the cycles progress, the features are reduced in amplitude, but a second peak is evident during the charge, matching the two-step reaction observed in discharge.

It should be noted that the periodic changes in capacity present in the 1C and 5C cycling data are correlated with the day / night cycles, causing small changes in temperature in our cycling setup. After the initial loss of capacity, the cathode cycles with 208 mAh/g (at 1C and 5C) of capacity without evidence of further degradation.

Figures 3(b) and 3(c) show potentiostatic EIS (PEIS) measurements taken every 5 cycles during 5C cycling for 460 cycles (cycling data shown in Supplementary Figure 7). Generally, a decrease in total impedance is observed over many cycles (Figure 3(b)). Figure 3(c) shows how the fitted resistance values for three identified contributions change over cycle number. Utilizing these three contributions allows for optimal fitting of the PEIS and GEIS data. The LiPON contribution represents the electrolyte resistance, RC1 and RC2 are two components attributed to charge transfer resistances of the cathode and/or its interfaces. The variations

observed in the LiPON resistance are attributed to small temperature changes as discussed above and can also be observed in RC1 and RC2. A small increase in the RC1 resistance is observed in the first 200 cycles, potentially signaling the formation of an interface layer that is detrimental for Li^+ conductivity to the cathode (or anode). The most significant contribution to impedance is observed for RC2, which shows a gradual decrease in resistance from roughly 120 to 60 kΩ during the first 200 cycles. This change correlates in cycle number with the initial capacity decay. While impedance decrease should not result in capacity fade directly, it may indicate restructuring of the cathode in a way that improves kinetics of conversion reaction at the cost of total capacity, observed as the amorphization of the cathode (Figure 3(d)).

We speculate that a coarsening of the cathode Cr and LiF nanodomains, is responsible for the observed loss of capacity in the first 200 cycles. In this way the LiF-Cr interfacial regions are reduced, leading to decreased material utilization due to slow diffusion of charge carriers and therefore reduced capacity. Direct evidence of the phase evolution is difficult to acquire as the active material layer is only 100 nm thick and buried under ∼3 µm of other materials. Based on the STEM-EDX results in Figure 3 and HR-TEM and FFT analysis (Supplementary Figure 8) we can identify that the particles inside the cathode become larger and more inhomogeneous. The increase in particle size is also associated with more crystalline nature of the layer. However, FFT analysis suggest little changes in the predominant lattice spacings, which can be assigned to the expected nanocrystalline Cr and LiF (measurements taken in the discharged state). (S)TEM experiments as a function of state-of-charge, aimed to identify the transition phases are beyond the scope of this communication and are the focus of our next manuscript.

Figure 3(d) shows STEM-EDX maps of the Cr-LiF cathode after 25 and 1564 cycles at 1C (the cycle numbers are indicated with stars on Figure 3(a)). After 1564 cycles, the particles become much larger, with Cr-rich or F-rich domains spanning a major fraction of the layer thickness. This might lead to improved kinetics mentioned earlier through percolation

pathways for electronic transport in the metal phase and ion transport in the LiF phase. However, this might also result in a reduction in available capacity as there would be fewer 'active' interfaces of Cr and LiF where conversion can happen with smaller overpotentials. Moreover, over the course of long-term cycling, Cr tends to accumulate at the interface with LiPON, likely related to the observation made for RC1 in Figure 3(b). We can speculate that the Cr is interacting with the electrolyte to form new inactive phases (CrO_x, $Cr(PO_4)_x$, etc.). Meanwhile, fluorine seems to accumulate on both interfaces (LiPON- and current collector-side). On the Ti current collector, likely a stable TiF_x phase forms that accumulates over thousands of cycles (also evidenced by the diffuse presence of Ti in the cathode shown in Figure 3(d). The fluorine accumulating towards the electrolyte side follows a similar trend to what was observed in our previous work.[21] Fluorine is observed accumulating towards the electrolyte interface, likely in the form LiF as this phase provides improved Li^+ conductivity in contrast to the metallic Cr phase. The Li+ conductive phase near the electrolyte and the e- conductive phase on the current collector side of the cathode lead to improved cathode transport properties, confirmed by the long term PEIS trends shown in Figure 3(c) and discussed previously.

3 Conclusions

The present study demonstrates a transition metal fluoride (TMF) conversion cathode in which the transition metal used is chromium. The lithiated (discharged) form of the chromium fluoride cathode (Cr:LiF 1.1:2) was tested in a thin-film, solid-state battery to isolate its performance from unwanted side reactions. We show that at a rate of C/10, the cathode exhibits an attractive specific capacity of 435 mAh/g and an energy density of 0.707 Wh/g (lithiated). The cathode also performs well at higher C-rates, consistently outperforming a Fe-LiF cathode manufactured in a similar way. Through computational and experimental investigations, we identified that the cathode likely converts to the CrF_2

phase upon charging (delithiation). Finally, a long term cycling study suggests the spontaneous formation of a new nanostructure which may have fast electrode kinetics albeit with less capacity as compared to the initial structure. Once this new structure is formed, the cathode exhibits very stable cycling for hundreds of cycles. This study provides the first demonstration of a chromium-based TMF cathode. With further fundamental understanding and material optimization, chromium-based fluorides could serve as a viable new class of high-energy TMF conversion cathodes for lithium-ion solid-state batteries.

4 Methods

4.1 Fabrication of Cells

Uncoated Corning® Boro-Aluminosilicate glasses (CB-0111, Delta Technologies, LTD., 25 mm x 25 mm x 1.1 mm) were coated with TiN with a thickness of 50 nm using a CT200 magnetron sputtering cluster (Alliance Concept) at 400 $°C$ by DC magnetron sputtering of a 25 cm diameter target of Ti (gas flow of 120 sccm Ar and 10 sccm N_2, working pressure of 3 mTorr) with a power of 3.1 W cm^{-2}. Ti was then deposited with a thickness of 200 nm using the same tool and target (21 sccm Ar gas flow, 2 W cm^{-2} power, and 3 mTorr pressure). The cathode was deposited to the desired thickness through a custom circular shadow mask (for 5 mm^2 cells) using a Nextdep thermal evaporator (Angstrom Engineering Inc.) by coevaporating Cr (99. 99%, 014760.18, Thermo Fischer Scientific Inc.) and LiF (99.99%, 014463.18, Thermo Fischer Scientific Inc.) inside Al_2O_3 crucibles (and a Ni crucible liner for LiF). The deposition rates of both materials were controlled during deposition using multiple quartz-crystal microbalances to achieve a stoichiometric ratio of 1.1:2 Cr:LiF and a total capacity of 1.02 μAh ($7.62*10^{-7}$ mol_{LiF} /cm^2, or 0.0204 mAh/cm^2). The solid electrolyte LiPON (N-doped Li_3PO_4) was deposited to a thickness of 1000 nm through a custom shadow mask using an Orion sputtering system (AJA International Inc.). LiPON was deposited using RF co-sputtering of Li_3PO_4 and Li_2O 2" targets in a confocal arrangement

at a gas flow of 50 sccm N_2, a power of 4.93 and 5.92 W cm^{-2}, respectively, and a working pressure of 3 mTorr. The Li metal (99+%, 211442500, Thermo Fischer Scientific Inc.) anode was deposited through a custom anode shadow mask using the same thermal evaporator as described above to a thickness of 2000 nm using an arc-coated stainless steel and alumina crucible.

4.2 Computational Methods

The electronic structure of atomic models was evaluated using density-functional theory (DFT) calculations using version 6.4.1 of the Vienna Ab-initio Simulation Package (VASP) package.[40–43] The r^{2}SCAN meta-GGA exchange-correlation functional was used due to its accuracy for a wide range of materials, including correlated systems that include transition metal ions.[31] The calculations were carried out using a plane-wave basis with a kinetic-energy cut-off of 520 eV, the Brillouin zone was sampled with a Monkhorst-Pack k-point grid with a maximal spacing of 0.25 $Å^{-1}$. Gaussian smearing of the electronic states was used with a width of 0.05 eV. The VASP recommended projector-augmented wave (PAW) sets were used for all elements. Electronic energies converged down to 10^{-6} eV during every self-consistent field (SCF) cycle using a preconditioned conjugated gradient algorithm (ALGO=ALL). Structures were optimized to a maximum force difference of 10^{-2} eV $Å^{-1}$ between ionic steps using a residual minimization method.

4.3 Characterization

Electrochemical characterization was performed in an Ar-filled glove box at room temperature with no applied cell pressure, utilizing Squidstat Plus for electrochemical impedance spectroscopy (EIS) and Squidstat Prime for direct current (DC) measurements (Admiral Instruments). Galvanostatic EIS with potential limitation experiments were conducted with a VMP-300 potentiostat (BioLogic). The reported capacities correspond to electrode-level capacities calculated using the measured thickness, area, and theoretical material densities

(Cr: 7.190 g/cm^3, LiF: 2.635 g/cm^3; assuming no porosity). Applied currents range from 1 $\mu A/cm^2$ to 100 $\mu A/cm^2$ in potential ranges from 0.5 to 5 V (vs Li^+/Li). Electrochemical impedance spectroscopy was conducted using a perturbation amplitude of 50 mV within a frequency range of 2 MHz to 0.5 Hz, with 12 steps per decade.

X-ray diffraction experiments were conducted using a Bruker D8 Discover instrument in grazing incidence mode, utilizing Cu Kα1 radiation. The experiments were performed at an incident angle of $\alpha = 0.3°$ and covered a measuring range of $2\theta = 30 - 70°$.

Heavy Ion ToF-ERDA (HI-ERDA) measurements were conducted with a 13 MeV iodine beam under a total scattering angle of 36° at the Laboratory of Ion Beam Physics at ETH Zurich.[44]

Samples for STEM-EDX were transferred to a Helios 660 (Thermo Fischer Scientific) FIB-SEM dual beam microscope without air exposure utilizing a transfer holder from Alemnis. The FIB-SEM was used to prepare TEM lamellae with a standard lift-out technique, but with an additional step of removing the Cu + Li layers at negative stage tilt to avoid issues with self-discharge and poor stability both mechanically and under the ion beam. The TEM lamellae were initially thinned using 30 kV Ga beam at a range of currents, followed by polishing at 8, 5 and 3 kV with lower ion beam currents until satisfactory electron beam transparency was achieved. The thinned lamellae were transferred without air exposure to an Ar filled glovebox for storage and then to a TEM with total ambient air exposure <5 minutes. The TEM experiments were performed on a JEOL JEM F200 microscope operated at 200 kV accelerating voltage, equipped with a dual EDX detector system. Pixel dwell time was kept around 10 μs, pixel size 1nm and beam current 65 pA.

TEM lamellae for STEM-EELS were prepared following the procedure described above, with the additional use of an air-free transfer TEM holder (Alemnis VTM, and Hummingbird Scientific 1580 Series) to ensure a fully airless transfer workflow. EELS measurements were performed on an analytical FEI Titan Themis operated at 300 kV, equipped with a CEOS Energy Filtering and Imaging Device (CEFID) spectrometer,[45,46] retrofitted with a hybrid-

pixel ELA detector (Dectris Ltd.).[47] The convergence and collection semi-angles were set to 24 and 26 mrad, respectively, yielding an effective collection semiangle of approximately 19 mrad for the inspected energy loss range. The electron beam was scanned across a 73x49 nm^2 area with a dwell time of 20 ms/pixel and a dispersion of 0.19 eV/channel.

Data Availability

The data that support the findings of this study are available from the author, Yaroslav E. Romanyuk (yaroslav.romanyuk@empa.ch), upon reasonable request.

Competing Interests

The authors declare no competing interests.

Author Contributions

J.C.: Conceptualization, Methodology, Validation, Formal Analysis, Investigation, Data Curation, Writing - Original Draft, Writing - Review and Draft, Visualization. J.M.: Conceptualization, Methodology, Investigation, Writing - Review and Editing, Visualization. V.M.: Investigation, Writing - Review and Editing, Visualization. F.C.M.: Investigation, Writing - Review and Editing, Visualization. A.M.: Investigation. M.H.F.: Writing - Review and Editing. M.D.R: Funding acquisition. M.S.I.: Writing - Review and Editing, Visualization, Funding acquisition. M.Y.: Writing - Review and Editing, Project administration. Y.E.R.: Conceptualization, Resources, Writing - Review and Editing, Visualization, Supervision, Project administration, Funding acquisition.

Acknowledgement

J.M. is supported by the European Union's Horizon 2020 research and innovation program (grant no. 95817) and the Swiss Federal Office of Energy (SFOE, grant no. SI/502460-01).V.M. and M.D.R. acknowledge support by the Swiss National Science Foundation (SNSF) under Project No. 200021_219706. F.C.M and S.I. are grateful to the Faraday Institution CATMAT project (EP/S003053/1, FIRG016) for financial support. M.H.F. is supported by a Rubicon Fellowship from the Netherlands Organization for Scientific Research (NWO).

The authors would like to acknowledge the use of the University of Oxford Advanced Research Computing (ARC) facility in carrying out this work.[48]

We thank the HEC Materials Chemistry Consortium (EP/R029431/1) for access and time on the Archer2 supercomputer facilities.

References

(1) Janek, J.; Zeier, W. G. A solid future for battery development. *Nature Energy* **2016**, *1*, 16141.

(2) Wu, R.; Bo, X.; Zhao, S.; Zhang, J.; Zhang, Q.; Jin, H.; Lin, Z.; Wang, S. Transition Metal Fluorides as Advanced Cathodes for Lithium/Sodium-Ion Batteries: Rational Enhancement Strategies and Underlying Electrochemical Mechanisms. *Advanced Functional Materials* **2025**, *35*, 2424603.

(3) Dayah, M. Periodic Table - Ptable. 1997; `https://ptable.com/`.

(4) Research, W. ElementData. 2014; `https://reference.wolfram.com/language/ref/ElementData.html`.

(5) Dong, K.; Dai, W.; Allison, J.; Viola, J.; Leah, Z. Metal Prices - Shanghai Metal Market. 2025; `https://www.metal.com`.

(6) Wu, F.; Yushin, G. Conversion cathodes for rechargeable lithium and lithium-ion batteries. *Energy & Environmental Science* **2017**, *10*, 435–459.

(7) Sun, L.; Li, Y.; Feng, W. Metal Fluoride Cathode Materials for Lithium Rechargeable Batteries: Focus on Iron Fluorides. *Small Methods* **2023**, *7*, 2201152.

(8) Yan, D.; Yang, H. Y.; Bai, Y. Tactics to optimize conversion-type metal fluoride/sulfide/oxide cathodes toward advanced lithium metal batteries. *Nano Research* **2023**, *16*, 8173–8190.

(9) Wang, X.; Wang, Z.; Chen, L.; Li, H.; Wu, F. High-capacity sulfide all-solid-state lithium battery with a conversion-type iron fluoride cathode. *Journal of Materials Chemistry A* **2023**, *11*, 4142–4154.

(10) Lai, C.; Chen, K.; Lei, M.; Hu, J.; Chen, S.; Li, C. Highly Reversible Iron Fluoride Conversion Cathodes Enabled by Deep-Eutectic Solvent Method and Heterostructure Design. *Advanced Functional Materials* **2024**, *34*, 2312415.

(11) Zhang, Y.; Chen, J.; Zhang, X.; Guo, B.; Yan, Z.; Liang, Y.; Sun, Y.; Xie, L.; He, X.; Gu, H.; Huang, J.; Huang, Q. Enabling Metal Fluorides Cathodes at Elevated Temperatures Using a Molten Salt Electrolyte. *Advanced Energy Materials* **2025**, *15*, 2500293.

(12) Xiao, A. W.; Lee, H. J.; Capone, I.; Robertson, A.; Wi, T.-U.; Fawdon, J.; Wheeler, S.; Lee, H.-W.; Grobert, N.; Pasta, M. Understanding the conversion mechanism and performance of monodisperse FeF2 nanocrystal cathodes. *Nature Materials* **2020**, *19*, 644–654.

(13) Omenya, F.; Zagarella, N. J.; Rana, J.; Zhang, H.; Siu, C.; Zhou, H.; Wen, B.; Chernova, N. A.; Piper, L. F. J.; Zhou, G.; Whittingham, M. S. Intrinsic Challenges to the Electrochemical Reversibility of the High Energy Density Copper(II) Fluoride Cathode Material. *ACS Applied Energy Materials* **2019**, *2*, 5243–5253.

(14) Zhao, Y.; Wei, K.; Wu, H.; Ma, S.; Li, J.; Cui, Y.; Dong, Z.; Cui, Y.; Li, C. LiF Splitting Catalyzed by Dual Metal Nanodomains for an Efficient Fluoride Conversion Cathode. *ACS Nano* **2019**, *13*, 2490–2500.

(15) Wang, F.; Kim, S.-W.; Seo, D.-H.; Kang, K.; Wang, L.; Su, D.; Vajo, J. J.; Wang, J.; Graetz, J. Ternary metal fluorides as high-energy cathodes with low cycling hysteresis. *Nature Communications* **2015**, *6*, 6668.

(16) Fan, X.; Zhu, Y.; Luo, C.; Gao, T.; Suo, L.; Liou, S. C.; Xu, K.; Wang, C. In situ lithiated FeF3/C nanocomposite as high energy conversion-reaction cathode for lithium-ion batteries. *Journal of Power Sources* **2016**, *307*, 435–442.

(17) Prakash, R.; Mishra, A. K.; Roth, A.; Kübel, C.; Scherer, T.; Ghafari, M.; Hahn, H.; Fichtner, M. A ferrocene-based carbon–iron lithium fluoride nanocomposite as a stable electrode material in lithium batteries. *Journal of Materials Chemistry* **2010**, *20*, 1871.

(18) Kim, S. W.; Nam, K. W.; Seo, D. H.; Hong, J.; Kim, H.; Gwon, H.; Kang, K. Energy storage in composites of a redox couple host and a lithium ion host. *Nano Today* **2012**, *7*, 168–173.

(19) Wu, T.; Cui, Y.; Wei, K.; Lai, C.; Zhao, Y.; Ni, S.; Chen, Y.; Gao, X.; Cui, Y.; Li, C. Catalysis of nickel nanodomains on Li-F dissociation for high-capacity fluoride cathodes with prior delithiation ability. *Nano Energy* **2022**, *103*, 107843.

(20) Wei, K.; Zhao, Y.; Chen, K.; Sun, K.; Wu, T.; Dong, Z.; Cui, Y.; Zeng, C.; Li, C. Low-Overpotential LiF Splitting in Lithiated Fluoride Conversion Cathode Catalyzed by Spinel Oxide. *Advanced Functional Materials* **2021**, *31*.

(21) Casella, J.; Morzy, J.; Gilshtein, E.; Yarema, M.; Futscher, M. H.; Romanyuk, Y. E. Electrochemical Activation of Fe-LiF Conversion Cathodes in Thin-Film Solid-State Batteries. *ACS Nano* **2024**, *18*, 4352–4359.

(22) Mishra, S.; Bharagava, R. N. Toxic and genotoxic effects of hexavalent chromium in environment and its bioremediation strategies. *Journal of Environmental Science and Health, Part C* **2016**, *34*, 1–32.

(23) Hope, E. G.; Levason, W.; Ogden, J. S. Is chromium hexafluoride octahedral? Experiment still suggests "yes!". *Inorganic Chemistry* **1991**, *30*, 4873–4874.

(24) Riedel, S.; Kaupp, M. The highest oxidation states of the transition metal elements. *Coordination Chemistry Reviews* **2009**, *253*, 606–624.

(25) Vanysek, P. Electrochemical series. *CRC handbook of chemistry and physics* **2000**, *8*, 8–33.

(26) Milazzo, G.; Caroli, S.; Braun, R. D. Tables of Standard Electrode Potentials. *Journal of The Electrochemical Society* **1978**, *125*, 261C–261C.

(27) Peng, J.; Wang, X.; Li, H.; Chen, L.; Wu, F. High-Capacity, Long-Life Iron Fluoride All-Solid-State Lithium Battery with Sulfide Solid Electrolyte. *Advanced Energy Materials* **2023**, *13*.

(28) Meng, Y.; Hu, J.; Lei, M.; Wu, H.; Qian, R.; Li, C. Synergistic Lewis Acid and Hydrogen Bonding Strategy to Enable Polymerized and Wide-Temperature Li-Fe-F Conversion Solid-State Batteries. *Advanced Energy Materials* **2025**, *15*.

(29) Wu, H.; Hu, J.; Yu, S.; Li, C. Heterostructure conductive interface and melt-penetration-bonding process to afford all-solid-state Li–FeF 3 garnet batteries with high cathode loading. *Energy & Environmental Science* **2025**, *18*, 923–936.

(30) Zagorac, D.; Müller, H.; Ruehl, S.; Zagorac, J.; Rehme, S. Recent developments in the Inorganic Crystal Structure Database: theoretical crystal structure data and related features. *Journal of Applied Crystallography* **2019**, *52*, 918–925.

(31) Furness, J. W.; Kaplan, A. D.; Ning, J.; Perdew, J. P.; Sun, J. Accurate and Numerically Efficient r 2 SCAN Meta-Generalized Gradient Approximation. *The Journal of Physical Chemistry Letters* **2020**, *11*, 8208–8215.

(32) Kirklin, S.; Meredig, B.; Wolverton, C. High-Throughput Computational Screening of New Li-Ion Battery Anode Materials. *Advanced Energy Materials* **2013**, *3*, 252–262.

(33) Lee, D. H.; Carroll, K. J.; Calvin, S.; Jin, S.; Meng, Y. S. Conversion mechanism of nickel fluoride and NiO-doped nickel fluoride in Li ion batteries. *Electrochimica Acta* **2012**, *59*, 213–221.

(34) Wang, F. et al. Conversion Reaction Mechanisms in Lithium Ion Batteries: Study of the Binary Metal Fluoride Electrodes. *Journal of the American Chemical Society* **2011**, *133*, 18828–18836.

(35) Hua, X. et al. Revisiting metal fluorides as lithium-ion battery cathodes. *Nature Materials* **2021**, *20*, 841–850.

(36) Maier, J. Thermodynamics of Electrochemical Lithium Storage. *Angewandte Chemie International Edition* **2013**, *52*, 4998–5026.

(37) Balaya, P.; Li, H.; Kienle, L.; Maier, J. Fully Reversible Homogeneous and Heterogeneous Li Storage in RuO 2 with High Capacity. *Advanced Functional Materials* **2003**, *13*, 621–625.

(38) Pearson, D. H.; Ahn, C. C.; Fultz, B. White lines and d -electron occupancies for the 3 d and 4 d transition metals. *Physical Review B* **1993**, *47*, 8471–8478.

(39) Daulton, T. L.; Little, B. J. Determination of chromium valence over the range Cr(0)–Cr(VI) by electron energy loss spectroscopy. *Ultramicroscopy* **2006**, *106*, 561–573.

(40) Kresse, G.; Hafner, J. Ab initio molecular dynamics for liquid metals. *Physical Review B* **1993**, *47*, 558–561.

(41) Kresse, G.; Furthmüller, J. Efficiency of ab-initio total energy calculations for metals and semiconductors using a plane-wave basis set. *Computational Materials Science* **1996**, *6*, 15–50.

(42) Kresse, G.; Furthmüller, J. Efficient iterative schemes for ab initio total-energy calculations using a plane-wave basis set. *Physical Review B* **1996**, *54*, 11169–11186.

(43) Kresse, G.; Joubert, D. From ultrasoft pseudopotentials to the projector augmented-wave method. *Physical Review B* **1999**, *59*, 1758–1775.

(44) Döbeli, M.; Kottler, C.; Glaus, F.; Suter, M. ERDA at the low energy limit. *Nuclear Instruments and Methods in Physics Research Section B: Beam Interactions with Materials and Atoms* **2005**, *241*, 428–435.

(45) Kahl, F.; Gerheim, V.; Linck, M.; Müller, H.; Schillinger, R.; Uhlemann, S. Test and characterization of a new post-column imaging energy filter. *Advances in Imaging and Electron Physics* **2019**, *212*, 35–70.

(46) Caridad, A. R.; Erni, R.; Vogel, A.; Rossell, M. D. Applications of a novel electron energy filter combined with a hybrid-pixel direct electron detector for the analysis of functional oxides by STEM/EELS and energy-filtered imaging. *Micron* **2022**, *160*, 103331.

(47) Plotkin-Swing, B.; Corbin, G. J.; Carlo, S. D.; Dellby, N.; Hoermann, C.; Hoffman, M. V.; Lovejoy, T. C.; Meyer, C. E.; Mittelberger, A.; Pantelic, R.; Piazza, L.; Krivanek, O. L. Hybrid pixel direct detector for electron energy loss spectroscopy. *Ultramicroscopy* **2020**, *217*, 113067.

(48) Richards, A. University of Oxford Advanced Research Computing. 2015; https://doi.org/10.5281/zenodo.22558.